

Effect of Incorporation of Calcium into Iron Carbonate Protective Layers in CO₂ Corrosion of Mild Steel

Saba Navabzadeh Esmaeely,^{‡,*} David Young,^{*} Bruce Brown,^{*} and Srdjan Nešić^{*}

ABSTRACT

The two dominant cationic species in reservoir brine are sodium (Na⁺) and calcium (Ca²⁺). Calcite (CaCO₃) and siderite (FeCO₃) are isostructural, thus Ca²⁺ incorporates readily into the hexagonal FeCO₃ lattice, and vice versa. In aqueous carbon dioxide (CO₂) solutions where both Ca²⁺ and ferrous iron (Fe²⁺) are present (such as downhole gas reservoirs or deep saline aquifers after CO₂ injection), inhomogeneous mixed metal carbonates with the formula Fe_xCa_yCO₃ (x + y = 1) can form; their presence on steel has been hypothesized to lead to localized corrosion. During carbon steel corrosion experiments conducted in electrolytes containing high Ca²⁺ concentrations, inhomogeneous corrosion product layers with the composition Fe_xCa_yCO₃ (x + y = 1) were indeed observed, along with non-uniform corrosion. Determining relative molar fractions of Ca²⁺ and Fe²⁺ in Fe_xCa_yCO₃ is paramount to predicting the relative properties and stability of such mixed metal carbonates. Using Bragg's law and equations to relate interplanar spacings to unit cell parameters, x-ray diffraction patterns yielded values for the mole fraction of Ca²⁺ in Fe_xCa_yCO₃. Procedures in the current study were designed to develop a range of specific corrosion product layers on mild steel samples. The compositional analysis of these surface layers was used to develop a relationship with the observed corrosion mechanisms. Experiments were conducted at constant chloride (Cl⁻) concentration with and without 10,000 ppm Ca²⁺ in stagnant conditions and for two different flow conditions. In stagnant conditions, localized corrosion was associated with the presence

of Ca²⁺ and the inhomogeneity of the corrosion product layer. The corrosion attack became uniform when flow was introduced.

KEY WORDS: calcium, CO₂ corrosion, FeCO₃, Fe_xCa_yCO₃, flow, localized

INTRODUCTION

The effect of calcium cations (Ca²⁺) on the formation and protectiveness of iron carbonate (FeCO₃) layers in aqueous carbon dioxide (CO₂) corrosion of mild steel was reported in a series of previous studies.¹⁻² These showed that the isostructurality of calcium carbonate (CaCO₃) and FeCO₃ allowed the incorporation of Ca²⁺ into the FeCO₃ structure; thus, the morphology and chemical properties of FeCO₃ were altered.

The importance of FeCO₃ formation on corrosion protection of mild steel has been well documented.³⁻¹⁴ In a stagnant aqueous CO₂ solution, the water chemistry at the corroding steel surface is not the same as the bulk water chemistry. As a consequence of the corrosion process that consumes hydrogen (H⁺) and releases ferrous iron (Fe²⁺) to the solution, the pH and Fe²⁺ concentration increase adjacent to the steel surface. This leads to a higher degree of FeCO₃ saturation near the steel surface and a higher probability of protective FeCO₃ layer formation. However, in a turbulent well-mixed solution, a corroding bare steel surface has almost the same water chemistry as the bulk solution, making protective FeCO₃ layer formation less probable.^{3,7,15-16} In addition, at very high flow rates, there is a possibility of removal of protective FeCO₃ layers, leading to localized corrosion.¹⁵⁻¹⁶

Submitted for publication: September 9, 2016. Revised and accepted: November 1, 2016. Preprint available online: November 1, 2016. <http://dx.doi.org/10.5006/2261>.

[‡] Corresponding author. E-mail address: sn294410@ohio.edu.

^{*} Institute for Corrosion and Multiphase Technology, Department of Chemical and Biomolecular Engineering, Ohio University, Ohio 45701.

The effect of Ca^{2+} in CO_2 corrosion of mild steel has been generally underestimated, and there is little consistent data reported. For example, Jiang, et al.,¹⁷ reported localized corrosion in CO_2 solutions containing calcium chloride (CaCl_2) and claimed that chloride ions (Cl^-) caused localized corrosion while Ca^{2+} delayed the initiation process; however, because of the short duration of experiments, it was unclear whether pit propagation was affected the same way. Ren, et al.,¹⁸ and Zhu, et al.,¹⁹ observed localized corrosion in CO_2 solutions containing CaCl_2 and also stated that this was a result of the presence of Cl^- , even if the experimental evidence did not allow them to distinguish the effect of Cl^- from that of Ca^{2+} . On the other hand, Gao, et al.,²⁰ reported that formation of “mixed” metal carbonates ($\text{Fe}_x\text{Ca}_y\text{CO}_3$ and $\text{Fe}_x(\text{Mg,Ca})_y\text{CO}_3$, where $x + y = 1$) in the precipitated layers was responsible for localized corrosion. Tavares, et al.,²¹ postulated that the mixed carbonate corrosion product layers are more porous than the iron carbonate layers. From this brief literature review, it remains unclear what mechanism is responsible for localized corrosion resulting from the presence of CaCl_2 in aqueous CO_2 solutions.

Therefore, the following questions are addressed in the present study:

1. Is it Cl^- or Ca^{2+} that leads to localized corrosion of mild steel in CO_2 solutions?
2. What is the effect of flow on the protectiveness of the precipitated $\text{Fe}_x\text{Ca}_y\text{CO}_3$ layer?
3. What is the exact composition of the $\text{Fe}_x\text{Ca}_y\text{CO}_3$ layers precipitated on the mild steel surface and how are they related to corrosion?

EXPERIMENTAL PROCEDURES

The test matrix is shown in Table 1. A conventional 2 L glass cell with a three-electrode electrochemical setup was used; the procedure was essentially the same as described in the previous study.¹ The main difference is related to the use of a magnetic stirrer to simulate flowing conditions in the glass cell. The desired Ca^{2+} concentration was obtained by addition of CaCl_2 . In order to have 10,000 ppm Ca^{2+} in the bulk solution, 54.7 g CaCl_2 was added to the cell. This

also meant that 17,800 ppm Cl^- was present in the bulk solution, which raised concerns that this concentration would affect corrosion rate, rather than Ca^{2+} . Therefore, a “baseline” experiment was also conducted with the same amount of Cl^- , but with no Ca^{2+} in the solution (in this case, the Cl^- concentration was achieved by adding NaCl).

A potentiostat was used to measure corrosion rate using the linear polarization resistance (LPR) method. Polarization resistance (R_p) was determined by specimen polarization ± 5 mV from the OCP at a scan rate of 0.125 mV/s. The measured R_p then was corrected for the solution resistance using electrochemical impedance spectroscopy measurement data at high frequencies (ca. 5 kHz).

Compositional analysis was performed by x-ray diffraction (XRD), using a $\text{CuK}\alpha$ source ($\lambda = 1.5405 \text{ \AA} = 0.1540 \text{ nm}$, 40 kV, and 44 mA), by scanning from 10 to 70 2θ at a scan rate of $1^\circ/\text{min}$. Scanning electron microscopy (SEM) and energy-dispersive x-ray spectroscopy (EDS) were used to characterize surface morphology and perform elemental analysis, respectively. Profilometry was used to investigate the mild steel surface, after the corrosion product layer was removed, for any indication of localized corrosion. Inductively coupled plasma spectroscopy was used to measure the Ca^{2+} concentration in samples of the aqueous solution. The Fe^{2+} concentration was measured by UV-vis spectrophotometry. To reveal the steel surface underneath the corrosion product layer, Clarke's solution (1,000 mL hydrochloric acid [HCl], 20 g antimony trioxide [Sb_2O_3], and 50 g stannous chloride [SnCl_2]) treatment was performed on one sample from each experiment, following the ASTM Standard G1 guidelines to remove the corrosion product layer.²²

RESULTS

Figure 1 shows the evolution of uniform corrosion rate over time for each test condition by LPR measurements; in all experiments the corrosion rate decreased over time. For two experimental conditions, the corrosion rate decreased and stabilized at

TABLE 1
Test Matrix

Parameters	Experiment 1 (baseline)	Experiment 2	Experiment 3	Experiment 4
Total pressure	0.1 MPa	0.1 MPa	0.1 MPa	0.1 MPa
$p\text{CO}_2$	0.05 MPa	0.05 MPa	0.05 MPa	0.05 MPa
Temperature	80°C	80°C	80°C	80°C
NaCl	4 wt%	1 wt%	1 wt%	1 wt%
Initial $[\text{Ca}^{2+}]^{(A)}$	0	10,000 ppm	10,000 ppm	10,000 ppm
Initial pH	5.5	5.3	5.5	5.5
Flow ^(B)	Stagnant	Stagnant	300 rpm	600 rpm
Steel	G10180	G10180	G10180	G10180

^(A) Ca^{2+} added as CaCl_2 .

^(B) A magnetic stirrer was used for solution agitation

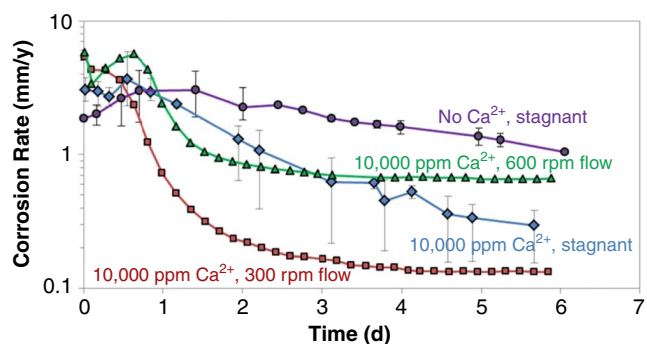


FIGURE 1. LPR uniform corrosion rate of mild steel exposed to a simulated brine solution with equal Cl^- concentrations with and without Ca^{2+} for different flow velocities at 80°C and $p\text{CO}_2$ of 0.05 MPa.

approximately 1 mm/y. This could be a result of formation of a partially protective layer. In the other two experiments, the corrosion rate decreased to less than 0.2 mm/y. In those experiments, a protective layer likely formed on the steel surface.^{7,10,23} In two of the four conditions, the experiments were repeated and the averages of the measured data, with error bars denoting the maximum and minimum deviation from the average, are reported here.

Based on the previous study conducted by the authors,¹ it was suspected that even when low general

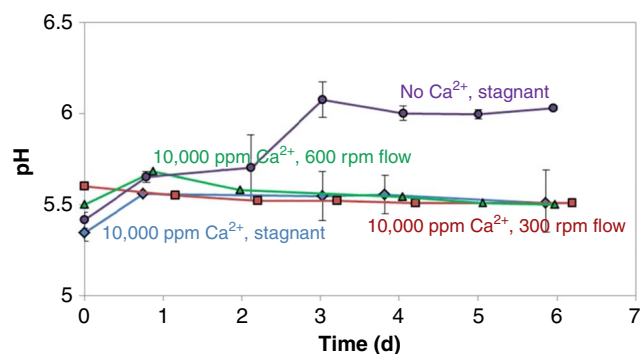


FIGURE 2. Variation of pH for a simulated brine solution with equal Cl^- concentrations with and without Ca^{2+} at different flow velocity at 80°C and $p\text{CO}_2$ of 0.05 MPa.

corrosion rates were detected by LPR, indicating a formation of a “protective layer,” there was a possibility of localized corrosion, which needed to be investigated. It was suggested that because of partial substitution of Fe^{2+} in the FeCO_3 lattice by Ca^{2+} , and vice versa, a mixed iron/calcium carbonate forms on the steel surface.^{1,24} This mixed carbonate layer is apparently not as protective as a pure FeCO_3 layer. This issue is further explored in the last section of this paper.

When steel corrodes in a limited volume aqueous CO_2 solution, it will typically lead to an increase of pH

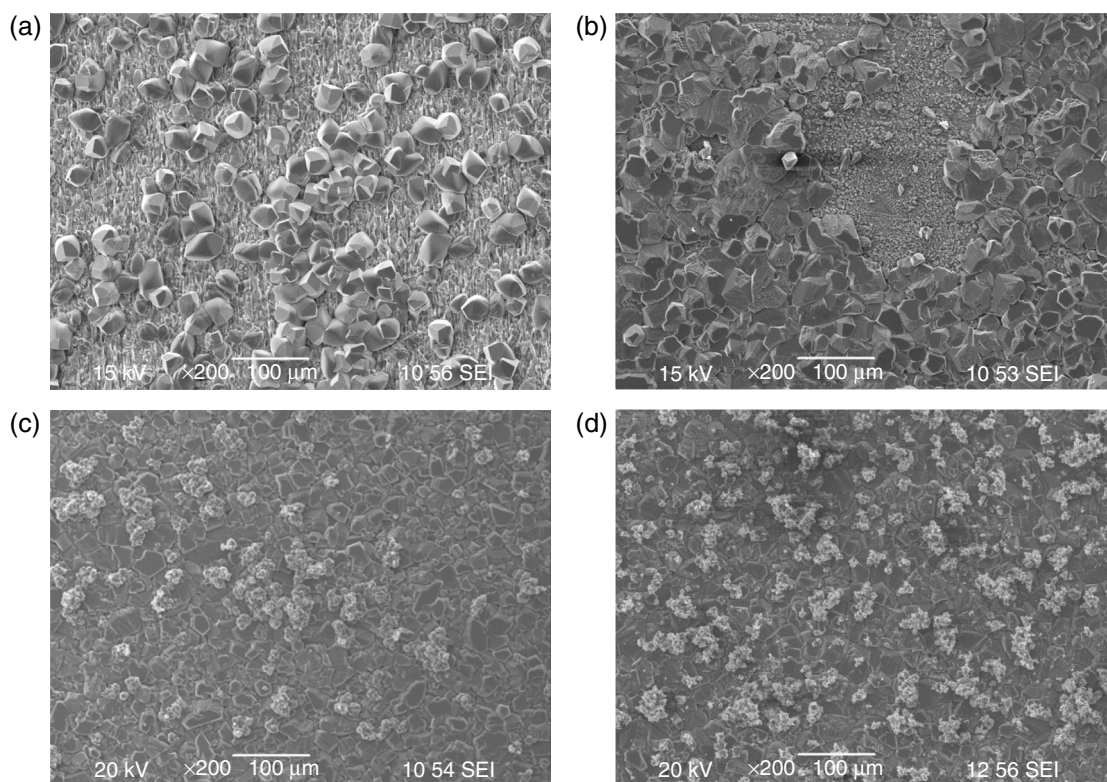


FIGURE 3. SEM images of samples (UNS G10180) removed after 6 d exposure to solutions at 80°C and $p\text{CO}_2$ of 0.05 MPa with: (a) 4 wt% NaCl in stagnant condition, (b) 10,000 ppm Ca^{2+} in stagnant condition, (c) 10,000 ppm Ca^{2+} at 300 rpm, and (d) 10,000 ppm Ca^{2+} at 600 rpm.

resulting from accumulation of corrosion products (increased Fe^{2+} concentration) over time. This is particularly true when solution volume to corroding steel surface area ratio is low, as was the case in the glass cell experiments presented here. ASTM Standard G31²⁵ advises at least 0.2 m ratio for the volume to steel surface area ratio, a value that was calculated to be close to 1 m in the current study, which is still a low value despite meeting the minimum requirement of the ASTM standard. Figure 2 shows that the pH for the baseline experiment (with no Ca^{2+}) increased during the first 3 d despite the periodic injections of deoxygenated diluted hydrochloric acid, which were done in order to try and maintain the pH. After 3 d, the pH increased and stabilized, being supersaturated with respect to FeCO_3 . The supersaturation leads to precipitation of solid FeCO_3 , and to solution acidification.¹ When the two processes achieve a balance (Fe^{2+} production by corrosion and Fe^{2+} depletion by precipitation), a stable pH is obtained, as seen in Figure 2.

Experiments that contained 10,000 ppm Ca^{2+} stayed stable at the initial pH of 5.5, without any pH adjustment. This was because of the equilibria associated with the aqueous species present, which autogenously maintained a pH of 5.5 throughout the experiment. Therefore, no significant precipitation of CaCO_3 was expected and consequently no solid CaCO_3 formation was visible in the glass cell. The initial CaCO_3 saturation degree was calculated to be 58 and over time it decreased to a value close to 3.

Figure 3 shows the SEM images of steel samples from each experiment after 6 d. The SEM images for the steel sample exposed to the baseline conditions (no Ca^{2+}) are shown in Figure 3(a) and show the corroded steel surface to be partially covered by FeCO_3 crystals, which are the only type of corrosion product layer that can form under these conditions.

The specimen exposed to 10,000 ppm Ca^{2+} (Figure 3(b)) shows a surface layer that did not have a uniform morphology either. However, it seems that there is a more compact layer adjacent to the steel surface, partially covered by clusters of larger crystals having a different appearance. The layer found on the samples retrieved from experiments with Ca^{2+} and different flow conditions are shown in Figures 3(c) and (d). The specimens were covered with a more compact layer of crystals with a different morphology. No significant difference is observed between these two specimens. This greater uniformity in the corrosion product layer on the specimens exposed to flow could be the result of a more homogeneous bulk solution which led to a more uniform water chemistry in the vicinity of the specimens.

In order to determine compositions of the layer on the steel specimens retrieved from solutions containing 10,000 ppm Ca^{2+} , XRD analysis was performed on

each. The results are shown in Figure 4. The most intense Bragg reflection for the isomorphous CaCO_3 and FeCO_3 phases corresponds to the [104] interplanar d-spacing, located at 29.42 2θ and 32.07 2θ , respectively.²⁶ In each of the XRD patterns, the [104] peak for FeCO_3 is shifted to a lower 2θ value, indicative of a larger d-spacing consistent with substitution of Fe^{2+} with the larger Ca^{2+} in equivalent lattice positions. Similarly, the [104] peak for CaCO_3 is shifted to a higher

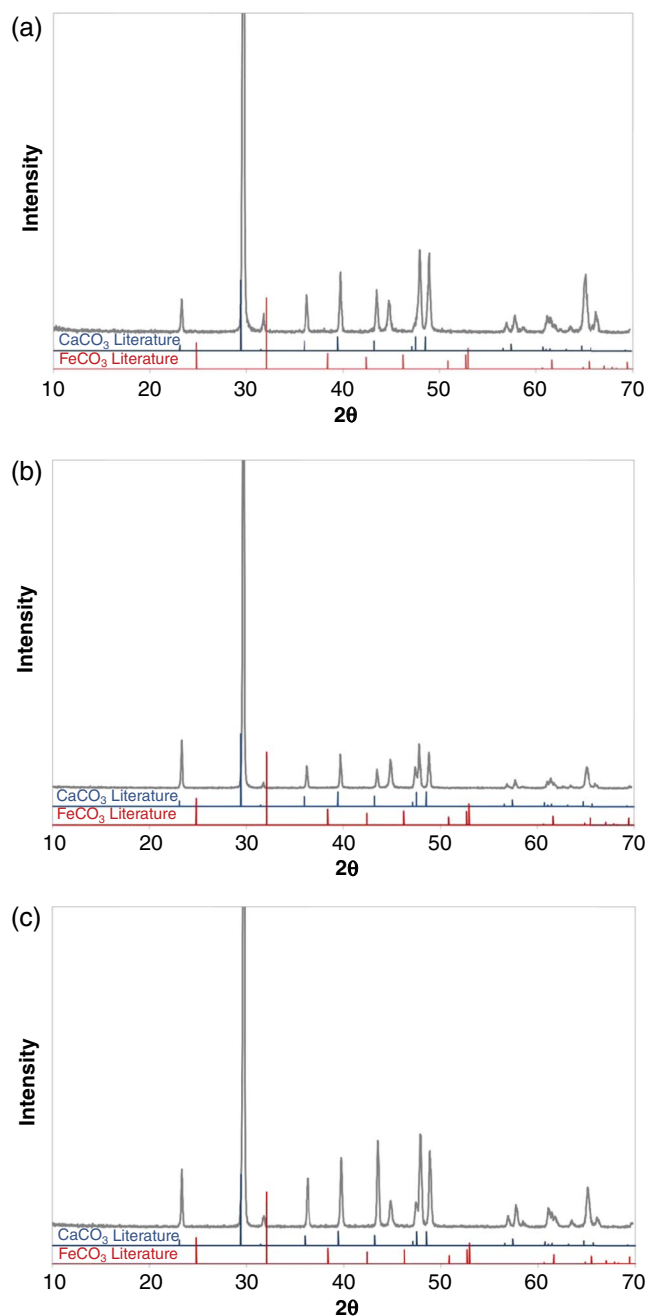


FIGURE 4. XRD patterns of samples (UNS G10180) after 6 d exposure to solutions at 80°C and $p\text{CO}_2$ of 0.05 MPa with (a) 10,000 ppm Ca^{2+} in stagnant condition, (b) 10,000 ppm Ca^{2+} at 300 rpm, and (c) 10,000 ppm Ca^{2+} at 600 rpm.

2 θ value, indicative of a smaller d-spacing consistent with substitution of Ca²⁺ with the smaller Fe²⁺ in equivalent lattice positions.

Figure 5 shows the cross-sectional analyses of the specimens after 6 d exposure to each test condition. Figure 5(a) shows a cross-sectioned area for the specimens retrieved from the 4 wt% NaCl solution. Figure 5(b) shows the cross-sectioned area of localized corrosion on the specimen surface for the experiment with 10,000 ppm Ca²⁺ at stagnant condition. Representative areas for each of the remaining two specimens are shown in the cross-sectional images in Figures 5(c) and (d) for the specimens exposed to 10,000 ppm Ca²⁺ at 300 rpm and 600 rpm, respectively. Localized corrosion was investigated further by study of the surface after the corrosion product layer was chemically removed with Clarke's solution.²²

Figure 6 shows the SEM images of the specimen surfaces after removal of the corrosion product or scale layer. Figures 6(b) and (c) show that the surface of the specimens exhibited features that could be consistent with localized corrosion. The surfaces of the specimens from the solutions with 4 wt% NaCl and with 10,000 ppm Ca²⁺ at 600 rpm flow did not reveal any such features. The pit penetration rate is calculated based on the maximum measured pit depth using profilometry, as shown in Figure 7. Using

Equation (1), the pit penetration rates (PPRs) were calculated to be 7.9 mm/y and 6.2 mm/y for the experiments with 10,000 ppm Ca²⁺ at stagnant condition and at 300 rpm, respectively. It is noteworthy that the pit propagation rate may vary with time as pits may become inactive. Pit propagation rate (PPR) investigation, which was not within the scope of the current study, demands longer duration experiment.

$$\text{PPR} = \frac{h \times 0.001 \times 365}{t \times 1} \quad (1)$$

where h is the deepest pit depth in μm , and t is the time in days.

MOLE FRACTION DETERMINATION OF CA²⁺ IN CA_xFE_yCO₃

The XRD patterns shown in Figures 4 and 8 can be used to calculate the concentration of Ca²⁺ in the lattice structure of the Ca_xFe_yCO₃ solid solution. Figure 9 shows the hexagonal Bravais lattice corresponding to the fundamental crystal structure of FeCO₃, CaCO₃, and Ca_xFe_yCO₃ ($x + y = 1$), as each phase is isostructural (calcite-type). Unit cell parameters a and c are calculated using Equation (2).²⁷ The value d in Equation (2) is calculated from Bragg's Law, shown in

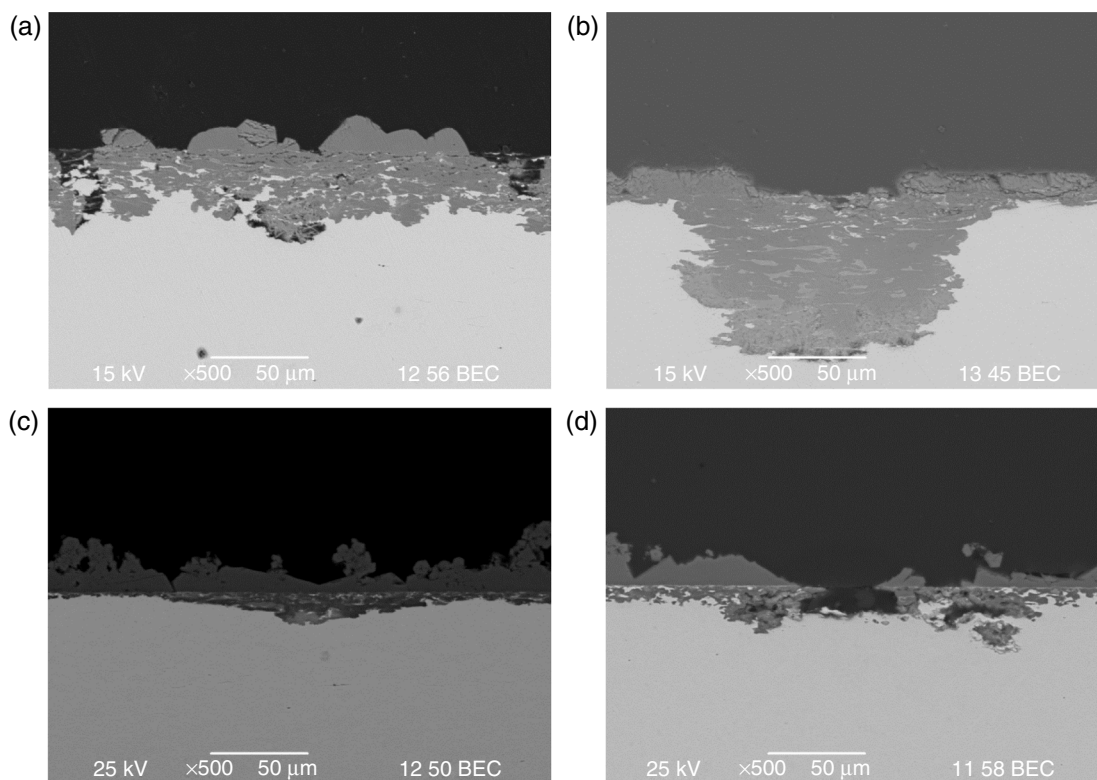


FIGURE 5. Cross-sectional images of specimens (UNS G10180) removed after 6 d exposure to solutions at 80°C and $p\text{CO}_2$ of 0.05 MPa with: (a) 4 wt% NaCl in stagnant condition, (b) 10,000 ppm Ca²⁺ in stagnant condition, (c) 10,000 ppm Ca²⁺ at 300 rpm, and (d) 10,000 ppm Ca²⁺ at 600 rpm.

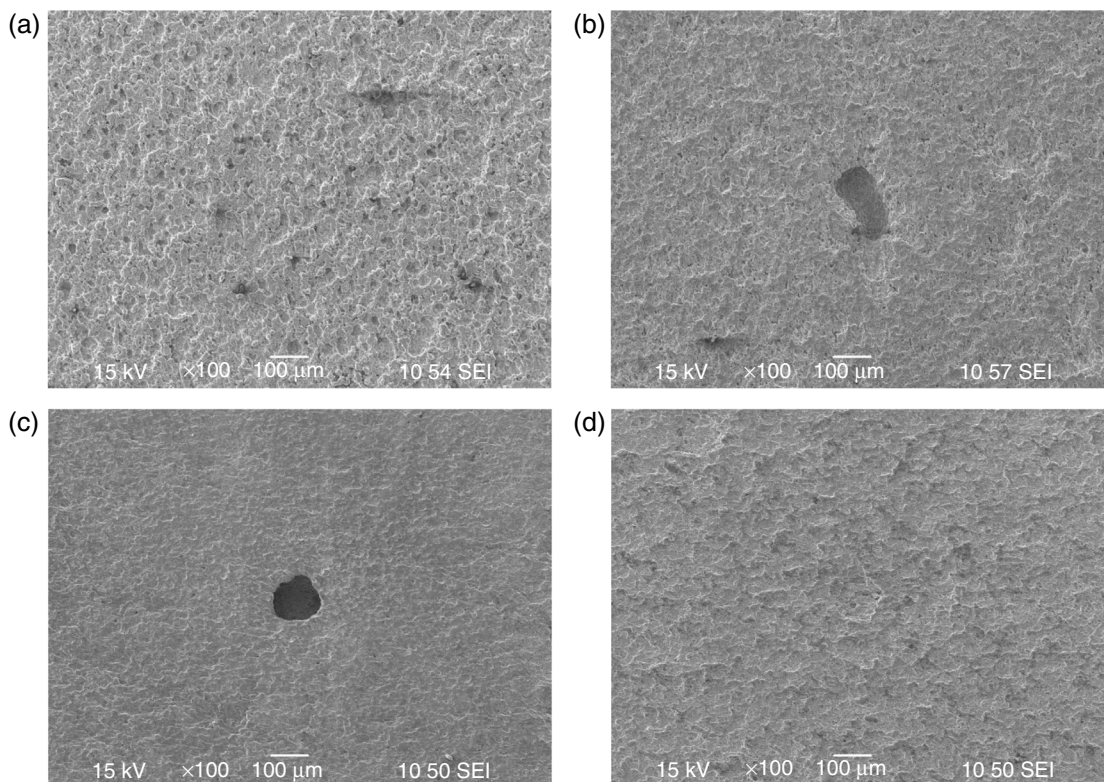


FIGURE 6. Surface after corrosion product removal (UNS G10180) after 6 d exposure to solutions at 80°C and $p\text{CO}_2$ of 0.05 MPa with: (a) 4 wt% NaCl in stagnant condition, (b) 10,000 ppm Ca^{2+} in stagnant condition, (c) 10,000 ppm Ca^{2+} at 300 rpm, and (d) 10,000 ppm Ca^{2+} at 600 rpm.

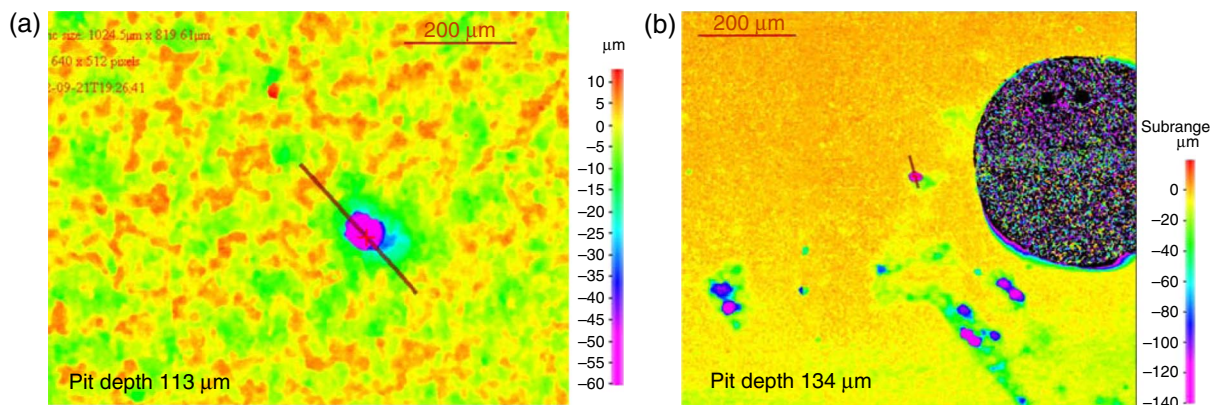


FIGURE 7. Profilometry image of a specimen (UNS G10180) after removal of corrosion product for the experiment conducted at 80°C and $p\text{CO}_2$ of 0.05 MPa with: (a) 10,000 ppm Ca^{2+} in stagnant condition, and (b) 10,000 ppm Ca^{2+} at 300 rpm.

Equation (3).²⁷ The a and c unit cell edges are determined using h , k , and l values, the Miller indices, corresponding to particular lattice planes associated with peaks in the acquired XRD data, recorded at 2θ values and converted to d (d -spacings), using Equation (3). The V unit cell volume is calculated from a and c using Equation (4). Assuming linear behavior for Ca^{2+} incorporation in the structure as regards the

unit cell parameters and the unit cell volume, the mole fraction x of Ca^{2+} in the solid solution $\text{Ca}_x\text{Fe}_y\text{CO}_3$ ($x + y = 1$) is found using Equation (5).²⁷ Figure 10 shows the plotted x values versus c for the specimens generated in the current study, as well as select literature data.²⁶ The calculated unit cell parameter c for each tested condition is located on the line in Figure 10, and the corresponding mole fraction x of Ca^{2+} is

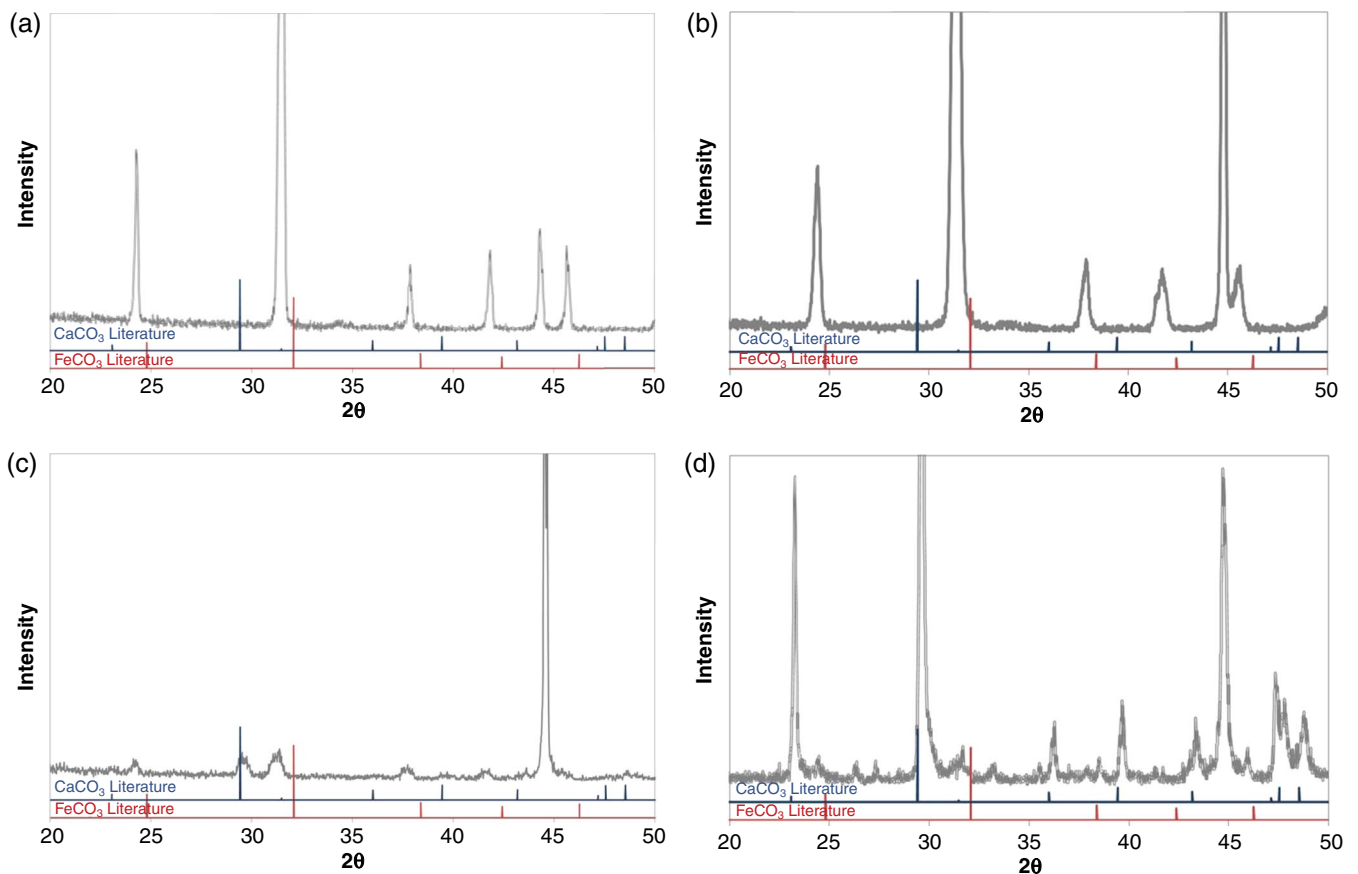


FIGURE 8. XRD patterns of samples (UNS G10180) after 6 d exposure at stagnant condition at 80°C and $p\text{CO}_2$ of 0.05 MPa with 10 ppm Fe^{2+} , initial pH 6.6, (a) 10 ppm Ca^{2+} , (b) 100 ppm Ca^{2+} , (c) 1,000 ppm Ca^{2+} , and (d) 10,000 ppm Ca^{2+1} .

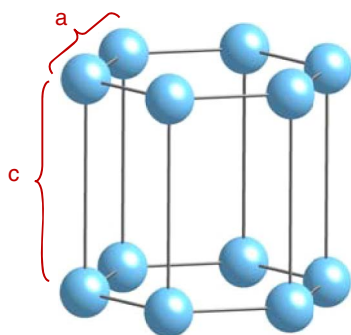


FIGURE 9. Hexagonal Bravais lattice.

determined. The red points are data from the literature, and further validate the accuracy of the calculations.²⁸ The solid triangles are calculated data from the previous study using the XRD plots in Figure 10. The open circles are calculated unit cell parameters from the current study using XRD patterns from Figure 4. Figure 11 shows the x value versus the unit cell volume. The same procedure was followed to find the x value for each tested condition using the unit cell volume. The same procedure can be used to calculate unit cell

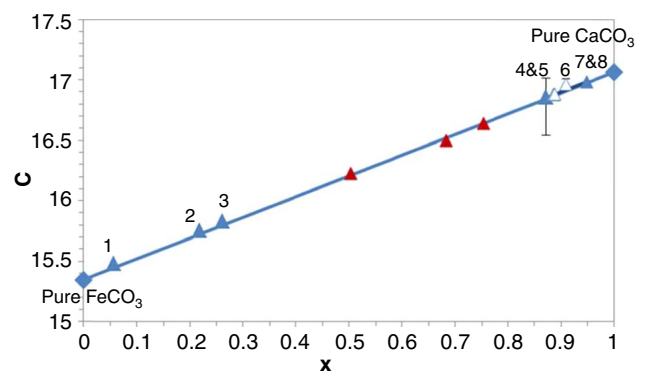


FIGURE 10. Unit cell parameter c versus the concentration of Ca^{2+} in the solid solution for experiments with: (1) 10 ppm Ca^{2+} , pH 6.6, and no flow; (2) 100 ppm Ca^{2+} , pH 6.6, and no flow; (3) and (7) 1,000 ppm Ca^{2+} , pH 6.6, and no flow; (4) 10,000 ppm Ca^{2+} , pH 5.5 at 300 rpm; (5) 10,000 ppm Ca^{2+} , pH 5.5 at 600 rpm; (6) 10,000 ppm Ca^{2+} , pH 5.5, and no flow; and (8) 10,000 ppm Ca^{2+} , pH 6.6, and no flow.

parameter a , and to find the corresponding x value, but the value a is smaller, and the calculation error is greater for the extracted values. Table 2 shows the results of the calculations. The x value was verified

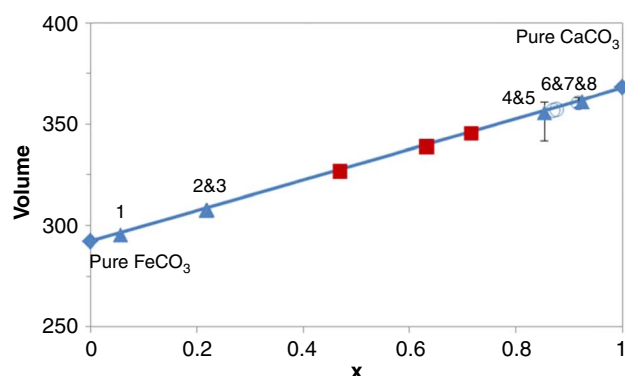


FIGURE 11. Unit cell volume versus concentration of Ca^{2+} in solid solution for experiments with: (1) 10 ppm Ca^{2+} , pH 6.6, and no flow; (2) 100 ppm Ca^{2+} , pH 6.6, and no flow; (3) and (7) 1,000 ppm Ca^{2+} , pH 6.6, and no flow; (4) 10,000 ppm Ca^{2+} , pH 5.5 at 300 rpm; (5) 10,000 ppm Ca^{2+} , pH 5.5 at 600 rpm; (6) 10,000 ppm Ca^{2+} , pH 5.5, and no flow; and (8) 10,000 ppm Ca^{2+} , pH 6.6, and no flow.

using EDS spectra using the ratio of Ca^{2+} at% to the summation of Fe^{2+} and Ca^{2+} at%. The deviation in the x value using EDS spectra and XRD pattern are likely related to a $\text{Ca}^{2+}/\text{Fe}^{2+}$ concentration gradient within the layer on the surface, as was shown in the EDS line scanning in the previous study.¹ The peaks on the XRD plots are asymmetric, which is also indicative of concentration gradients within the solid solution. The onset of diffraction for the [104] Bragg reflections occurred between $29\ 2\theta$ and $32\ 2\theta$. This is indicative of the presence of compositions ranging from pure calcium carbonate, mixed calcium iron carbonates, and pure iron carbonate. The shape of the peak is indicative of the relative concentrations of iron and calcium, and the existence of concentration gradients. If the area close to $29\ 2\theta$ is larger than the area on the tail side of the peak (close to $32\ 2\theta$), the mixed carbonate contains more Ca^{2+} than Fe^{2+} and vice versa.

$$\frac{1}{d^2} = \frac{4}{3} \left(\frac{h^2 + hk + k^2}{a^2} \right) + \frac{l^2}{c^2} \quad (2)$$

$$d = \frac{n\lambda}{2 \sin \theta} \quad (3)$$

$$V = \frac{\sqrt{3}}{2} a^2 c \quad (4)$$

$$y = 1.6885x + 15.373 \quad (5)$$

ANALYSIS

Based on the results shown above, the authors are now in the position to try and answer the three questions posed at the beginning of the article.

1. Is it Cl^- or Ca^{2+} that leads to localized corrosion of mild steel in CO_2 solutions? From Figure 6 it is apparent that in the experiment where there was no Ca^{2+} in the solution (Figure 6[a]), there was no localized corrosion. In the equivalent experiment that contained Ca^{2+} , localized corrosion was observed, suggesting that the cause of localized corrosion is related to the presence of Ca^{2+} rather than Cl^- .
2. What is the effect of flow on the protectiveness of the precipitated $\text{Fe}_x\text{Ca}_y\text{CO}_3$ layer? Referring to Figure 1, it is seen that flow affects the general corrosion rates: when at stagnant condition and low velocity, a low corrosion rate is seen as a result of formation of a possible protective layer (see Figure 3), while at higher velocity a high corrosion rate is obtained. However, at stagnant condition and low velocity localized corrosion is observed (see Figure 6), suggesting that only a partially protective layer was formed. There was no localized corrosion at high velocity when an unprotective layer formed.
3. What is the exact composition of the $\text{Fe}_x\text{Ca}_y\text{CO}_3$ layers precipitated on the mild steel surface

TABLE 2

Composition of the $\text{Ca}_x\text{Fe}_y\text{CO}_3$ Solid Solutions

Flow Condition	Initial Ca^{2+} (ppm)	Weight Loss Corrosion (mm/y)	Localized Corrosion (mm/y)	Calculated x from EDS Spectra	Calculated x from XRD Patterns Using "c"	Calculated x from XRD Patterns Using "V"	$\text{Ca}_x\text{Fe}_y\text{CO}_3$ ($x+y=1$)
Previous Study							
Stagnant	10	0.6	—	0.045	0.05	0.05	$\text{Ca}_{0.05}\text{Fe}_{0.95}\text{CO}_3$
	100	NA	—	0.22	0.22	0.22	$\text{Ca}_{0.22}\text{Fe}_{0.78}\text{CO}_3$
	1,000	1.3	—	(A)	0.25	0.21	$\text{Ca}_{0.25}\text{Fe}_{0.75}\text{CO}_3$
				(A)	0.94	0.91	$\text{Ca}_{0.94}\text{Fe}_{0.06}\text{CO}_3$
10,000	0.7	6.0	0.91	0.86	0.84	$\text{Ca}_{0.86}\text{Fe}_{0.14}\text{CO}_3$	
Current Study							
Stagnant	10,000	0.8	7.9	0.96	0.91	0.91	$\text{Ca}_{0.91}\text{Fe}_{0.09}\text{CO}_3$
300 rpm	10,000	0.5	6.2	0.94	0.88	0.87	$\text{Ca}_{0.88}\text{Fe}_{0.12}\text{CO}_3$
600 rpm	10,000	1.2	—	0.91	0.88	0.87	$\text{Ca}_{0.88}\text{Fe}_{0.12}\text{CO}_3$

(A) As previously reported,¹ the steel surface is covered with a bilayer at this Ca^{2+} concentration, so calculating the x value based on EDS data would not be representative.

and how is it related to corrosion? The exact composition of the $\text{Fe}_x\text{Ca}_y\text{CO}_3$ layers was reported in Table 2. In the case of a monolayer, it seems that the higher mole fraction of Ca^{2+} could potentially lead to localized corrosion. However, it remains unclear why the condition with 600 rpm did not suffer any localized corrosion.

CONCLUSIONS

❖ A mixed layer of $\text{Ca}_x\text{Fe}_y\text{CO}_3$ ($x + y = 1$) was detected on a steel surface exposed to a solution containing Ca^{2+} and aqueous CO_2 , resulting from the isostructurality of CaCO_3 and FeCO_3 . In some of these conditions (in the presence of high concentration of CaCl_2), localized corrosion was observed. Additional experimentation showed Ca^{2+} to be responsible for initiation of localized corrosion rather than the Cl^- . It was shown that flow affects the layer formation. The more agitated solution led to a less protective $\text{Ca}_x\text{Fe}_y\text{CO}_3$ layer. Using XRD patterns and EDS spectra, mole fraction (x) values for Ca^{2+} in $\text{Ca}_x\text{Fe}_y\text{CO}_3$ ($x + y = 1$) were independently calculated. When the mole fraction of Ca^{2+} in the $\text{Ca}_x\text{Fe}_y\text{CO}_3$ ($x + y = 1$) unit cell was close to one, the protectiveness conferred to steel by the layer was diminished.

ACKNOWLEDGMENTS

The authors would like to thank the Center for Electrochemical Engineering Research at Ohio University for the use of the XRD instrumentation. The support of the Department of Chemical & Biomolecular Engineering at Ohio University is appreciated.

REFERENCES

1. S. Navabzadeh Esmaeely, Y. Choi, D. Young, S. Nešić, *Corrosion* 69 (2013): p. 912-920.
2. S. Navabzadeh Esmaeely, Y. Choi, D. Young, S. Nešić, *MP* 53 (2014): p. 1-6.
3. A. Dugstad, "Mechanism of Protective Film Formation During CO_2 Corrosion of Carbon Steel," CORROSION 1998, paper no. 31 (Houston, TX: NACE International, 1998).
4. J.K. Heuer, J.F. Stubbs, *Corros. Sci.* 41 (1999): p. 1231-1243.
5. M.B. Kermani, A. Morshed, *Corrosion* 59 (2003): p. 659-683.
6. S. Nešić, L. Lunde, *Corrosion* 50 (1994): p. 717-727.
7. S. Nešić, "Carbon Dioxide Corrosion of Mild Steel," in *Uhlig's Corrosion Handbook*, ed. R.W. Revie (Hoboken, NJ: John Wiley & Sons, 2011), p. 229-245.
8. C.A. Palacios, J.R. Shadley, *Corrosion* 47 (1991): p. 122-127.
9. J. Han, S. Nešić, Y. Yang, B. Brown, *Electrochim. Acta* 56 (2011): p. 5396-5404.
10. M. Nordsveen, S. Nešić, R. Nyborg, A. Stangeland, *Corrosion* 59 (2003): p. 443-456.
11. V. Ruzic, M. Veidt, S. Nešić, *Corrosion* 62 (2006): p. 598-611.
12. K. Videm, A. Dugstad, *MP* 28, 3 (1989): p. 63.
13. K. Videm, A. Dugstad, *MP* 28, 4 (1989): p. 46.
14. L. Sanders, "An Integrated Study of Corrosion and Scale Interactions in the Absence and Presence of Combined Chemicals" (Ph.D. diss., University of Leeds, 2014).
15. S. Nešić, *Energy Fuels* 26 (2012): p. 4098-4111.
16. R. Nyborg, A. Dugstad, "Initiation and Growth of Mesa Corrosion Attack During CO_2 Corrosion of Carbon Steel," CORROSION 1998, paper no. 29 (Houston, TX: NACE, 1998).
17. X. Jiang, Y.G. Zheng, D.R. Qu, W. Ke, *Corros. Sci.* 48 (2006): p. 3091-3108.
18. C.Q. Ren, X. Wang, L. Liu, H.E. Yang, N. Xian, *Mater. Corros.* 63 (2012): p. 168-172.
19. S.D. Zhu, J.F. Wei, Z.Q. Bai, G.S. Zhou, J. Miao, R. Cai, *Eng. Fail. Anal.* 18 (2011): p. 950-962.
20. K. Gao, F. Yu, X. Pang, G. Zhang, L. Qiao, W. Chu, M. Lu, *Corros. Sci.* 50 (2008): p. 2796-2803.
21. L.M. Tavares, E.M. da Costa, J.J. de Oliveira Andrade, R. Hubler, B. Huet, *Appl. Surf. Sci.* 359 (2015): p. 143-152.
22. ASTM Standard G1 (Reapproved), "Standard Practice for Preparing, Cleaning, and Evaluating Corrosion Test" (West Conshohocken, PA: ASTM International, 1999).
23. S. Nešić, *Corros. Sci.* 49 (2007): p. 4308-4338.
24. B.F.M. Pots, S.D. Kapusta, "Prediction of Corrosion Rates of the Main Corrosion Mechanisms in Upstream Applications," CORROSION 2005, paper no. 550 (Houston, TX: NACE, 2005).
25. ASTM Standard G31 (Reapproved), "Standard Practice for Laboratory Immersion Corrosion Testing of Metals" (West Conshohocken, PA: ASTM International, 2004).
26. D. Barthelmy, "Mineralogy Database," Webmineral, 2012, <http://webmineral.com/>.
27. A.R. West, *Solid State Chemistry and Its Applications* (Aberdeen, Scotland: John Wiley & Sons, 1998), p. 694.
28. P.M. Davidson, G.H. Symmes, B.A. Cohen, R.J. Reeder, D.H. Lindsley, *Geochim. Cosmochim. Acta* 58 (1994): p. 5105-5109.